


Article

Study on Zinc-Modified Adsorbent for Adsorption of Trace CO₂ in Electronic Special Gas BF₃

Zhaochen Huang  and Guoqiang Huang *

School of Chemical Engineering and Technology, Tianjin University, Tianjin 300072, China; huangzc@tju.edu.cn

* Correspondence: hgq@tju.edu.cn; Tel.: +86-022-27891125

Abstract: Usually, the ion implantation gases used in semiconductor production are required to be extremely high in purity. Due to the presence of trace CO₂ in electronic special gas BF₃, the quality of the material is significantly affected, which makes it crucial to impose control on CO₂ content. Unlike a series of blank adsorbents reported in other studies, the zinc-loaded adsorbents prepared in this study are intended for the adsorption of CO₂ from CO₂/BF₃. Firstly, the materials were characterized by XRD, BET, SEM-EDS and TG-DSC analysis, etc., and the breakthrough curves of the adsorbents as obtained under different preparation conditions were investigated at 20 °C and 200 kPa. The results show that the adsorption performance reached the optimal level when the activation temperature was 450 °C and a 13X molecular sieve was impregnated by 0.15 mol/L Zn(NO₃)₂. Moreover, compared with the Zn-13X, the breakthrough time was reduced to 69% and 44% in two adsorption cycles, respectively. Finally, FTIR was used to reveal the adsorption mechanism of the carbonates produced by CO₂ adsorption. It was found that the adsorption performance was affected by the irreversible reduction in the number of active sites due to the continuous formation of polydentate carbonate during adsorption and regeneration.

Keywords: CO₂ adsorption; 13X molecular sieve; carbonate species



Citation: Huang, Z.; Huang, G. Study on Zinc-Modified Adsorbent for Adsorption of Trace CO₂ in Electronic Special Gas BF₃. *Processes* **2023**, *11*, 1075. <https://doi.org/10.3390/pr11041075>

Academic Editor: Farid B. Cortés

Received: 5 March 2023

Revised: 19 March 2023

Accepted: 27 March 2023

Published: 3 April 2023



Copyright: © 2023 by the authors. Licensee MDPI, Basel, Switzerland. This article is an open access article distributed under the terms and conditions of the Creative Commons Attribution (CC BY) license (<https://creativecommons.org/licenses/by/4.0/>).

1. Introduction

As the market demand for chips increases, the need for better performance and higher yields is also growing, which drives the rapid progress made in semiconductor manufacturing technology. Meanwhile, the advances in chip design have also led to a continuous increase in the demand for better chemicals. By the 1970s, ion implantation techniques had been widely applied because of their anisotropy, the alignment of source and leak poles, and the accurate control of nodule depth and doping concentration [1]. As a commonly used P-type dopant source, BF₃ is also a strong Lewis acid that hydrolyzes rapidly after coming into contact with water to form HF. Research by C. Graham calculated the quadrupole moment of BF₃ to be $12.6 \times 10^{-40} \text{ cm}^2$ (20 °C) [2]. Due to the electron-deficient structure of the central B atom, B forms complexes with atoms containing single electron pairs instantly. In some studies, it has been indicated that the order of affinity strengths of BF₃ with Lewis bases is as follows: amine > ether > aldehyde > nitrile > carbon monoxide [3]. As a Lewis base, CO₂ can form a Lewis acid-base adduct with BF₃ [4]. Figure 1 shows the form of BF₃ complexes with CO₂. The CO₂ in BF₃ used for ion implantation can introduce carbon impurities into wafers, increasing the leakage current of gate oxides and severely affecting the electrical properties of the device. Additionally, the introduction of carbon impurity leads to a poor uniformity of the radial resistivity of silicon, which significantly decreases the breakdown voltage of the device, resulting in greatly reducing the lifetime of the device [5].

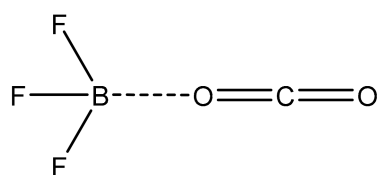


Figure 1. Structure of the $\text{BF}_3\text{-CO}_2$ complex.

The mainstream method used for the industrial production of BF_3 is fluoroborate pyrolysis [6]. However, this method tends to introduce various impurities into BF_3 , including SiF_4 and CO_2 , which are difficult to remove. Fortunately, SiF_4 can be removed through reduced pressure distillation, but CO_2 is non-existent in the liquid phase at atmospheric pressure. If we rely solely on distillation to remove CO_2 , the liquid phase would develop only when the pressure exceeds the three-phase point (527 kPa). In this case, it remains necessary to make a difference between the boiling point and freezing point of CO_2 by increasing the pressure for sufficient distillation. However, high pressure distillation not only increases the cost of various equipment such as compressors and other pressure transmission devices but also narrows the boiling point difference between BF_3 and SiF_4 , making it more difficult to remove the impurities. Therefore, other purification methods must be used as well to remove CO_2 from BF_3 .

The common methods used to remove CO_2 in industrial settings include absorption and adsorption [7]. Under the absorption method, thermoalkaline solutions such as hot potassium carbonate or organic amine solutions are commonly used for the absorption of CO_2 . However, this method is unsuited to the removal of CO_2 from BF_3 systems due to the strong reactivity and affinity of BF_3 to water and amine. Adsorption is considered a simple and inexpensive way to remove CO_2 . The solid adsorbents commonly used for CO_2 removal include zeolites [8–11] and metal-organic framework materials [12–14]. The adsorption of CO_2 from BF_3 with activated carbon has been proposed [15], but after adding activated carbon, the concentration of CO_2 decreased only from 200 ppm to 150 ppm. The patent mentions the adsorption of CO_2 and SiF_4 from BF_3 at low temperatures with zeolites such as 4A/5A/13X [16,17]. In order to ensure the separation effect, it is necessary to carry out a low-flow rate adsorption operation, but this will generate adsorption accumulation of heat, leading to a non-continuous operation. However, these adsorbents all rely only on the basicity of the zeolite or the well-developed pore structure of the activated carbon, which leads to a low capacity for the adsorption of CO_2 by this system.

Additionally, when CO_2 concentrations are low, relying solely on physical adsorption can result in extremely poor adsorption capacities due to insufficient mass transfer propulsion. This problem can be effectively reduced by means of chemical adsorption. Fatemeh Fashi et al. loaded piperazine onto a 13X zeolite to produce excellent performance in CO_2 adsorption from the air and natural gas [18]. Su-Kyung Lee et al. prepared nitrogen-doped microporous carbon with a high N content, which showed high CO_2 adsorption capacity for $\text{CO}_2\text{-H}_2\text{O-N}_2$ mixtures [19]. However, as mentioned above, BF_3 shows a very strong affinity for amine groups, and this method may cause competitive adsorption and unsatisfactory adsorption performance when used in the CO_2/BF_3 system. An efficient solution to this problem is alkali metal oxide loading, which relies on adsorption to generate the carbonates, such as chemisorption. Research by M. Kato et al. used lithium orthosilicate to achieve a high saturation adsorption capacity at room temperature and high temperatures under 500 ppm and a 2% CO_2 concentration [20]. The macro-porous K_2CO_3 -doped Li_4SiO_4 pellets were used to adsorb CO_2 at 580 °C, and better cycling stability was obtained [21]. Madhavi Jonnalagadda et al. showed that porous carbon-supported calcium oxide can be used for the adsorption and separation of CO_2 in CH_4/CO_2 systems at 25 °C [22]. Fan Wang et al. applied mesoporous magnesium oxide-alumina composites to CO_2 capture at 25 °C [23]. Pang, H., et al. prepared a $\text{MgO-Na}_2\text{CO}_3\text{-KNO}_3$ adsorbent for CO_2 adsorption at 400–480 °C, and the adsorbent showed excellent cycling stability [24]. Nevertheless, the adsorption performance of these metal oxides is still unsatisfactory at low temperatures.

It cannot match well with the low-temperature distillation process of BF_3 in terms of process energy consumption. ZnO supported activated carbon [25], mesoporous GO-ZnO nanocomposites [26], and activated carbon modified by ZnCl_2 [27] exhibited excellent adsorption properties at 40 °C, 25 °C and 0 °C, respectively.

Therefore, this paper aims to develop an inexpensive and readily available adsorbent that can be used to remove CO_2 using a zinc metal salt modifying carrier with good adsorption performance for the CO_2/BF_3 system. By exploring the optimum preparation conditions of a series of adsorbents, the performance of modified adsorbents was significantly improved compared with that of blank adsorbents. In this study, the modified adsorbent was initially used in the CO_2/BF_3 system. At the same time, the materials were characterized by XRD, BET, SEM-EDS, TG-DSC analysis, etc., and the adsorption performances of the adsorbents were measured. Finally, the regeneration adsorption performance of the adsorbent was explored, and the changes in carbonate species on the surface of the adsorbent were revealed through FTIR during the adsorption and regeneration processes.

2. Materials and Methods

2.1. Adsorbent Preparation

Commercial zeolite 4A (diameter: 3–5 mm), zeolite 5A (diameter: 3–5 mm), zeolite 13X (diameter: 3–5 mm), activated alumina (diameter: 3–5 mm), and activated carbon (rod, $\Phi 1.5$) were used as the carriers of active components. $\text{ZnSO}_4 \cdot 7\text{H}_2\text{O}$ (99%) was provided by Tianjin Damao Chemical Reagent Factory, Tianjin, China; ZnAc_2 (99%) was provided by Shanghai Aladdin Biochemical Technology Co., Ltd, Shanghai, China. and ZnCl_2 and $\text{Zn}(\text{NO}_3)_2$ standard solutions (1 mol/L) were provided by Shenzhen Bolinda Technology Co., Ltd, Shenzhen, China. During the process of preparation, the original carrier was washed twice with distilled water and then heated in a drying oven at 110 °C for 2 h to remove all potential impurities. After the optimal carrier was determined, it was immersed in the zinc metal salt solution for 6 h at 20 °C. Afterwards, the samples were dried at 110 °C for 4 h, heated to 450 °C for 2 h for activation, and then stored under anhydrous conditions. Finally, the adsorbent samples modified by ZnSO_4 , ZnAc_2 , ZnCl_2 and $\text{Zn}(\text{NO}_3)_2$ were obtained, respectively.

2.2. Characterization of Adsorbents

To measure the pore size, pore volume and specific surface area of the adsorbents, nitrogen adsorption was performed at 77.4 K using a surface analyzer (ASAP 2460, Micromeritics Instrument Corporation, Atlanta, GA, USA). Additionally, the specific surface area was calculated by the BET method. The crystal structures of adsorbents loaded with different zinc salts were determined through X-ray diffraction (Bruker D8 advance, Bruker Corporation, Billerica, MA, USA). X-rays were produced with $\text{Cu K}\alpha$ at a scanning speed of 1°/min, and 2θ ranged from 10° to 70°. For an analysis of mass changes in modified adsorbent during calcination, the simultaneous thermal analyzer (STA 449F3 Jupiter, NETZSCH-Gerätebau GmbH, Bavaria, Germany) was used. The simultaneous thermal analysis was carried out at a rate of 10 °C/min from 50 °C to 600 °C in a nitrogen atmosphere. Fresh, post-adsorbed and regenerated adsorbents were analyzed by means of Fourier transform infrared spectroscopy (Nicolet iS10, Thermo Fisher Scientific Inc., Waltham, MA, USA). The morphology of the adsorbent surface and the elemental distribution on it were observed using SEM-EDS (JEOL JSM-IT200, JEOL Japan Electronics Co., Ltd., Shoshima City, Tokyo, Japan).

2.3. CO_2 Adsorption Experiments

The gas mixtures of BF_3 (800 ppm), CO_2 (200 ppm), N_2 (99.9%) and N_2 (99.999%) were provided by Dalian Daito Gas Co., Ltd. (Dalian, China) and Ningbo Linde Gas Co., Ltd. (Ningbo, China), respectively. As BF_3 is highly toxic and extremely corrosive when reacting with water, the raw gas used for this experiment was diluted with N_2 to reduce the safety risk of the experiment. To prevent the entry of moisture from the air into the equipment,

positive pressure was maintained inside. The adsorbents used in this study were filled to 1 g in an adsorptive column with a diameter of 10 mm and a length of 450 mm. Adsorption experiments were performed at a pressure of 200 kPa, with the operating temperature set to 20 °C and the volumetric flow rate of the feed gas maintained at 60 mL/min. The adsorption temperature was controlled by using the refrigerant coil and electric heating jacket of the adsorption column. The CO₂ concentration at the column outlet was measured using a CO₂ detector tube sourced from Kitagawa Corporation, Japan. Figure 2 shows a schematic diagram of the adsorption system. To facilitate the experiment, adsorption breakthrough was defined as when the CO₂ concentration at the outlet reached 80% of the feed, which is 160 ppm.

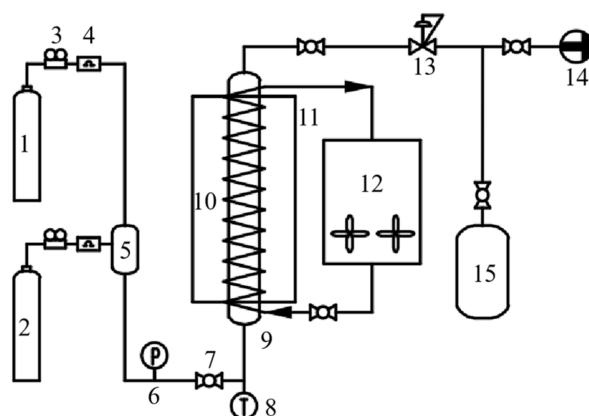


Figure 2. Adsorption system: (1) N₂; (2) blended gases; (3) pressure reducing valve; (4) mass flow meters; (5) buffer tanks; (6) pressure gauge; (7) valve; (8) thermocouple; (9) adsorptive column; (10) refrigerant coils; (11) heating jackets; (12) circulating refrigeration pumps; (13) back pressure valve; (14) sampling port; and (15) exhaust gas tank.

After loading the adsorbent each time, the column temperature was raised to 150 °C, purged with N₂, and maintained for 2 h. The purpose of this was to remove water from the adsorbent. The column temperature was reduced to the experimental temperature, and nitrogen gas was converted into BF₃ gas for the adsorption experiment. After the adsorption experiment breakthrough, the gas path was switched to N₂ purge for 2 h, thus avoiding contact with moisture in the air when the adsorbent was removed and HF was generated.

3. Results and Discussion

3.1. Optimization of Preparation Conditions

3.1.1. Optimal Carrier

The blank 4A, 5A, 13X, alumina, and activated carbon blank carriers were comparatively measured with a pH meter at a carrier-to-water mass ratio of 1:3. Table 1 lists the pH values of the different blank carriers.

Table 1. pH values of the different blank carriers.

Sample	4A	5A	13X	Al ₂ O ₃	Activated Carbon
pH	9.59	9.68	10.67	9.23	7.10

As observed, the relative alkalinity of 13X is the strongest. The alkalinity of these carriers is contributed to by the presence of their internal hydroxyl groups, and the strength of the alkalinity is positively related to the number of internal hydroxyl groups. The adsorption caused by the interaction between CO₂ and hydroxyl is attributed to physical adsorption, and a larger number of alkaline carriers can improve CO₂ adsorption performance. Comparing the three molecular sieves in the sample, the 13X molecular sieve has

the strongest polarity. This is due to CO₂ having a strong quadrupole moment, which leads to a stronger affinity with 13X of stronger polarity [28]. Furthermore, microporous structures are a key feature of efficient CO₂ adsorption, and the pore size is particularly important for the adsorption performance [29]. The pore size range of 13X is around 0.8–1 nm, which is larger than 5A (~0.5 nm) and 4A (~0.4 nm). The larger pore size of 13X makes the adsorption of CO₂ less affected by the steric effect.

In order to investigate their effects on CO₂ removal, comparative adsorption experiments on blank carriers (4A, 5A, 13X, Al₂O₃, and activated carbon) were performed at 20 °C. It was revealed that the purification performance of blank 13X was significantly higher compared to other blank carriers.

According to the experimental results shown in Figure 3, the breakthrough curves of all the blank carriers varied significantly, all the blank carriers showed a breakthrough in the dynamic adsorption experiments at 20 °C before 150 min, and the effective adsorption time of 13X approached 150 min when 160 ppm of CO₂ at the export of the column was defined as the breakthrough point. This time is much longer than 30 min as the breakthrough time of activated carbon. In CH₄/CO₂ and N₂/CO₂ systems, 13X also achieved better CO₂ adsorption performance than the other molecular sieves. Allowing for this set of controlled trials, 13X was determined as the optimal carrier.

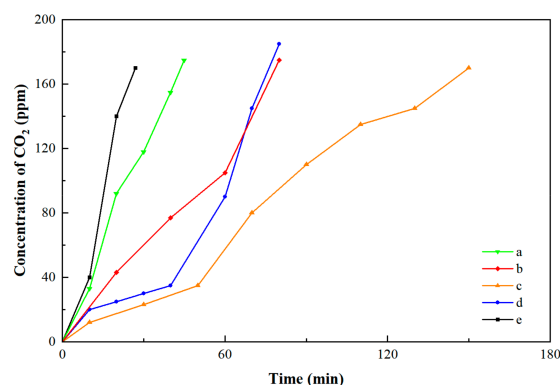


Figure 3. Breakthrough curves of blank carriers were compared at 20 °C: (a) 4A, (b) 5A, (c) 13X, (d) Al₂O₃ and (e) activated carbon, respectively.

3.1.2. Selection of the Optimum Load

The crystal structures of blank 13X, ZnCl₂-13X, ZnAc₂-13X, Zn(NO₃)₂-13X and ZnSO₄-13X were comparatively measured by X-ray diffraction (XRD) in the 2θ range of 10–70° to analyze the impact of ZnCl₂, ZnAc₂, Zn(NO₃)₂ and ZnSO₄ on adsorbents. Figure 4 shows the XRD patterns of the fresh adsorbent samples with all the major characteristic peaks. The zinc load on the adsorbent sample is detailed in Table 2.

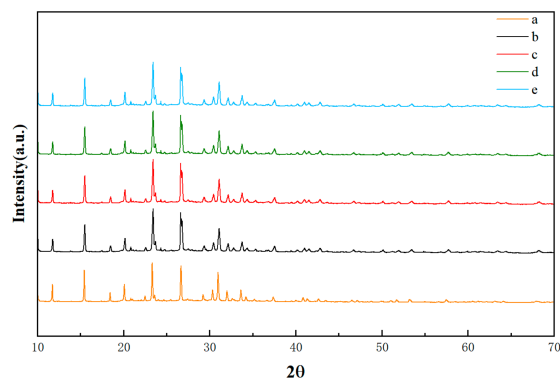


Figure 4. XRD patterns of blank 13X and modified 13X: (a) blank 13X, (b) ZnCl₂-13X, (c) ZnAc₂-13X, (d) Zn(NO₃)₂-13X and (e) ZnSO₄-13X, respectively.

Table 2. Elemental composition after modification of 13X with different zinc salts.

Sample ¹	ZnCl ₂ -13X	ZnAc ₂ -13X	Zn(NO ₃) ₂ -13X	ZnSO ₄ -13X
C element load/wt.%	12.15	12.86	9.61	12.45
N element load/wt.%	0.00	0.00	0.10	0.00
O element load/wt.%	35.77	38.91	38.31	35.08
Na element load/wt.%	5.86	3.37	5.17	4.69
Mg element load/wt.%	0.00	2.01	1.59	0.93
Al element load/wt.%	10.74	11.93	12.12	11.69
Si element load/wt.%	20.13	24.34	21.07	19.92
S element load/wt.%	0.00	0.00	0.00	0.91
K element load/wt.%	0.78	0.39	0.44	0.37
Ca element load/wt.%	0.49	0.48	1.01	0.66
Ti element load/wt.%	0.12	0.26	0.00	0.31
Fe element load/wt.%	1.65	2.67	1.65	1.95
Zn element load/wt.%	12.30	2.80	8.94	11.06

¹ The impregnation solutions were all 0.1 mol/L.

As observed, these adsorbents maintained the characteristic peaks of blank 13X, suggesting that the major blank 13X structure was intact after the loading of these zinc compounds. The presence of zinc in other adsorbents in these samples was confirmed by Energy Dispersive Spectroscopy (EDS). However, the zinc content in ZnAc₂-13X was found to be significantly lower compared to the other adsorbents, reaching a mass percentage of only 2.80%. This is because the activation temperature of the experiment reaches above the boiling point of ZnAc₂, which leads to sublimation during the calcination process. The decomposition temperature of zinc sulfate is very high, which makes it difficult to decompose at the experimental activation temperature. ZnCl₂ loading caused significant changes to the structure of 13X zeolite [30]. Therefore, Zn(NO₃)₂-loaded zinc is incorporated into the 13X structure or exists in the form of oxides, and the particle size is too small to reach the detection limit of XRD, indicating the widespread distribution of zinc species. Additionally, it can be seen from the data in Table 2 that even when Zn(NO₃)₂ is loaded with 13X, the residual content of N element on 13X after calcination is extremely low. This phenomenon can also be obtained from Table 3. This indicates that Zn(NO₃)₂ has been adequately decomposed in the calcination process. Moreover, an investigation was conducted into the effects of different zinc salt loadings on the adsorption performance of 13X. Figure 5 shows the results of the adsorption breakthrough experiments on different zinc salts loaded with 13X.

Table 3. Elemental composition after modification of 13X with different Zn(NO₃)₂ solution concentrations.

The Concentration of Impregnating Solution/(mol·L ⁻¹)	0	0.05	0.1	0.15	0.2	0.3	0.4
C element load/wt.%	7.76	9.31	9.61	9.01	11.25	11.12	11.56
N element load/wt.%	0.00	0.00	0.10	0.00	0.00	0.19	0.00
O element load/wt.%	52.34	45.46	38.31	44.17	45.35	38.89	43.81
Na element load/wt.%	8.48	7.08	5.17	5.99	5.66	5.78	5.63
Mg element load/wt.%	1.07	1.35	1.59	1.31	1.33	1.52	1.17
Al element load/wt.%	10.90	10.48	12.12	10.77	9.15	10.76	8.96
Si element load/wt.%	17.42	17.14	21.07	17.75	16.18	18.98	17.17
K element load/wt.%	0.00	0.00	0.44	0.00	0.00	0.42	0.00
Ca element load/wt.%	0.83	0.62	1.01	0.54	0.41	0.95	0.39
Fe element load/wt.%	1.19	1.31	1.65	1.37	1.09	1.62	1.25
Zn element load/wt.%	0.00	7.24	8.94	9.07	9.58	9.78	10.06

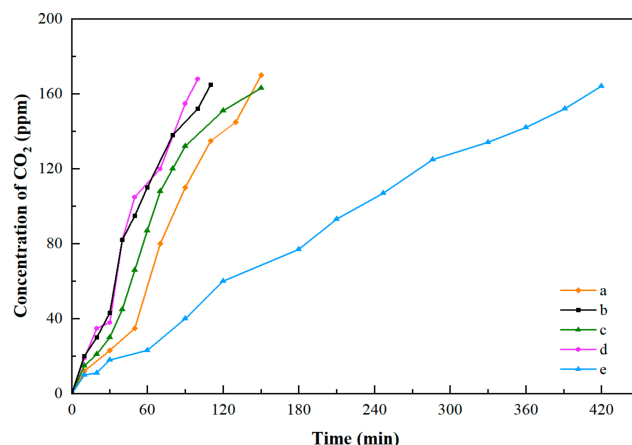


Figure 5. Breakthrough curves of blank 13X and modified 13X were compared at 20 °C: (a) blank 13X, (b) ZnCl₂-13X, (c) ZnAc₂-13X, (d) ZnSO₄-13X and (e) Zn(NO₃)₂-13X, respectively.

Apparently, only 13X loaded with Zn(NO₃)₂ produced an optimal effect, with the breakthrough time of the adsorbent being close to 420 min. As for the other three salts loaded with 13X, they exerted a negative effect on adsorption. It can be concluded from this set of experimental results that, among these four zinc salts, only Zn(NO₃)₂ is suitable for loading.

3.1.3. Optimization of Impregnation Concentration

According to the results of EDS listed in Table 3, the content of zinc loaded on 13X rises with an increase in the concentration of the impregnating solution. However, the growth rate is low after the concentration of the impregnating solution exceeds 0.2 mol/L.

Furthermore, the results of scanning electron microscopy (SEM) were obtained, as shown in Figure 6. When the concentration of the impregnating solution is less than or equal to 0.15 mol/L, the surface loading of the molecular sieve is more uniform. However, the surface of the molecular sieve stuck together at high loading concentrations, which is evident when the concentration of the impregnating solution reaches 0.4 mol/L.

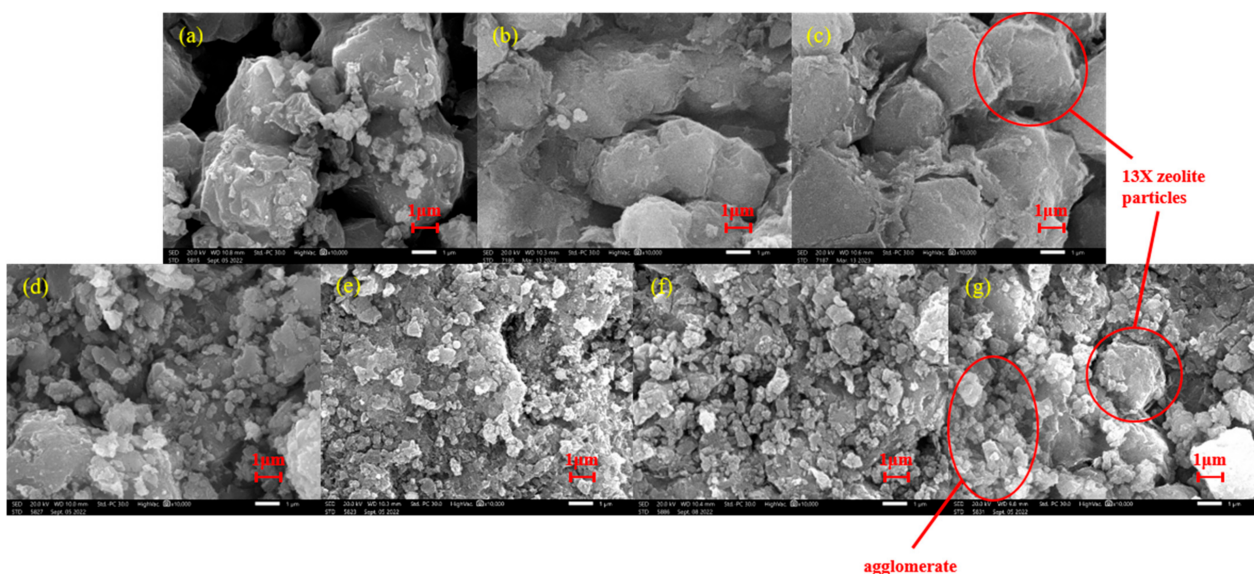


Figure 6. SEM images of the adsorbent with the impregnating solution concentration of (a) 0 mol/L, (b) 0.05 mol/L, (c) 0.1 mol/L, (d) 0.15 mol/L, (e) 0.2 mol/L, (f) 0.3 mol/L and (g) 0.4 mol/L, respectively.

Table 4 shows the physical properties of the adsorbents with different modifications. It can be seen from the table that there is a decrease in both the specific surface area and total pore volume of 13X after zinc modification. This is because the act of impregnation loads new substances on the surface of the molecular sieve, which reduces the specific surface area and pore volume of the molecular sieve while reducing the pore size. The specific surface area and total pore volume of the adsorbent show a gradual decline. Judging from the SEM results, the degree of agglomeration on the surface of the molecular sieve increases when the concentration of the impregnating solution exceeds 0.2 mol/L. For this modification process of $\text{Zn}(\text{NO}_3)_2$ impregnated with 13X, the concentration of the impregnating solution is a significant influencing factor. When the concentration of the impregnating solution exceeds a certain level, the load accumulates on the surface of the molecular sieve, thus reducing its porous properties.

Table 4. Specific surface area, total pore volume and average pore diameter of $\text{Zn}(\text{NO}_3)_2$ modified 13X with different concentrations.

The Concentration of the Impregnating Solution (mol·L ⁻¹)	Specific Surface Area (m ² /g)	Total Pore Volume (cm ³ /g)	Average Pore Size (nm)
0	388	0.243	12
0.05	384	0.237	12
0.1	347	0.238	11
0.15	315	0.214	11
0.2	288	0.202	11
0.3	280	0.202	11
0.4	265	0.207	12

$\text{Zn}(\text{NO}_3)_2$ in the concentration range of 0.05–0.4 mol/L was used to modify 13X by means of impregnation, and dynamic adsorption experiments were conducted on the modified adsorbent, the results of which are shown in Figure 7.

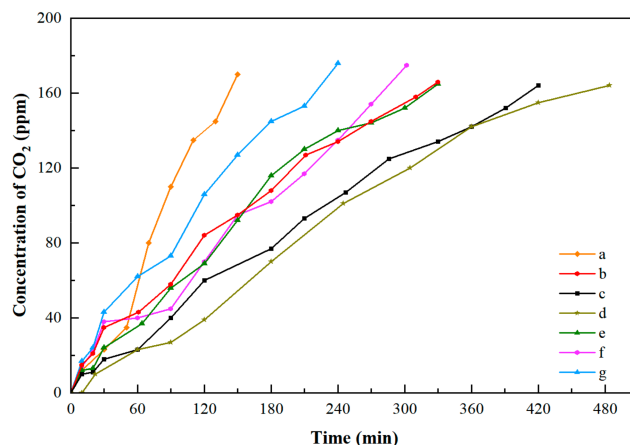


Figure 7. Breakthrough curves of different $\text{Zn}(\text{NO}_3)_2$ concentrations of impregnating solution are compared at 20 °C: (a) blank, (b) 0.05 mol/L, (c) 0.1 mol/L, (d) 0.15 mol/L, (e) 0.2 mol/L, (f) 0.3 mol/L and (g) 0.4 mol/L, respectively.

From the above experimental results, it can be concluded that the adsorbents modified by 0.05–0.4 mol/L zinc nitrate impregnation achieved better adsorption performance than the blank 13X. The breakthrough time of the adsorbents first increased and then decreased with the increase of the impregnating solution concentration, reaching a maximum at 0.15 mol/L. At this time, the breakthrough time of the adsorbent reaches 480 min, which is over two times higher than compared to the blank carrier. For the adsorbent impregnated at 0.15 mol/L, the adsorption effect was more significant than that of the adsorbent impregnated at 0.05 mol/L, but the other properties, such as the specific surface area, were inferior

to the latter. This is accounted for by the results shown in Table 3 and Figure 6, where the loading of zinc in the 0.15 mol/L impregnated adsorbent is higher. This concentration falls below the threshold for agglomeration to occur on the surface of the molecular sieve. Thus, it can be concluded that 0.15 mol/L is the optimal concentration of the impregnating solution under the current experimental conditions.

3.1.4. Optimization of Activation Temperature

The simultaneous thermal analysis (TG-DSC) of the dried uncalcined adsorbent was conducted after impregnation, as shown in Figure 8. It can be seen from the figure that the rate of weight loss declines after the temperature rises to 180 °C. The weight loss of the samples prior to this temperature largely results from the loss of water from crystallization in the samples. The decomposition of the loadings continues when the temperature ranges between 180 and 415 °C, at which point the zinc oxides are gradually produced. The DSC curve shows that the sample is in a state of significant heat uptake until 415 °C, indicating the occurrence of a decomposition reaction within the sample. The decreasing rate of heat uptake indicates that the decomposition reaction is coming to an end at this temperature. As the temperature continues to rise, the mass of the adsorbent continues to decrease, and heat absorption continues, which is accompanied by a slow loss of mass. This results mainly from the dehydration of the hydroxyl groups of the molecular sieve by condensation at high temperatures.

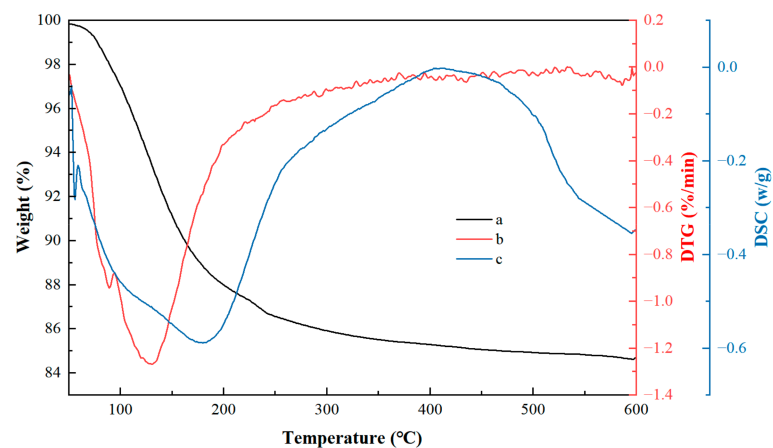


Figure 8. TG-DSC curve of $\text{Zn}(\text{NO}_3)_2\text{-13X}$: (a) TG curve, (b) DTG curve and (c) DSC curve.

Figure 9 shows the results of adsorption breakthrough experiments conducted at an activation temperature ranging from 350 to 550 °C. The concentration of $\text{Zn}(\text{NO}_3)_2$ during the process of adsorbent modification is 0.15 mol/L in all cases.

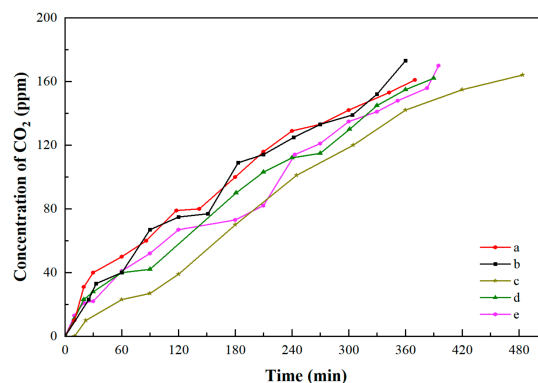


Figure 9. Comparison of breakthrough curves of $\text{Zn}(\text{NO}_3)_2\text{-13X}$ at 20 °C for different activation temperatures: (a) 350 °C, (b) 400 °C, (c) 450 °C, (d) 500 °C and (e) 550 °C, respectively.

As observed, the breakthrough time increases and then decreases with the activation temperature, reaching a peak at 450 °C. The breakthrough time under this experimental condition approaches 480 min. It can also be ascertained that the adsorption performance of all five of the modified adsorbents significantly improves over the blank 13X molecular sieve. Notably, the experimental results shown in Figure 9 suggest that even the sample calcined at 350 °C can achieve an optimized adsorption effect compared with the blank 13X. That is to say, zinc oxides were formed on the molecular sieve even at an activation temperature of 350 °C, except that the loaded zinc compounds were not decomposed completely to form zinc oxides. In these samples, the zinc compounds in the adsorbents with an activation temperature of no less than 415 °C have basically been decomposed into zinc oxides. In addition, the results in Figure 8 show that the heat absorption rate occurs at low temperature levels ranging from 415 to 450 °C. Judging from the experimental results in Figure 9, 450 °C is the ideal activation temperature. Based on the above analysis, it can be determined that the adsorbent modification conditions are optimum, with 0.15 mol/L solution of $\text{Zn}(\text{NO}_3)_2$ used to impregnate 13X at an activation temperature of 450 °C. The adsorbent is denoted as Zn-13X.

3.2. Stability Evaluation of Adsorbents

In order to further explore the adsorption mechanism of the adsorbent and to evaluate the stability of the adsorbent, regeneration experiments and Fourier-transform infrared spectroscopy of the adsorbent were carried out under the optimal conditions described above. The regeneration of the adsorbent was carried out by purging at 450 °C in the presence of pure N_2 for 2 h. The results of these regeneration experiments are shown in Figure 10.

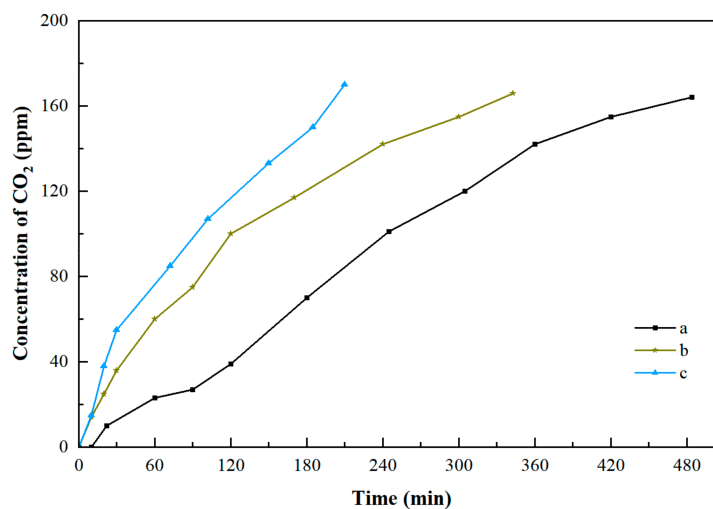


Figure 10. Breakthrough curves of Zn-13X at 20 °C, where (a) fresh adsorbent, (b) once regeneration adsorbent and (c) twice regeneration adsorbent, respectively.

According to the experimental results shown in Figure 10, the breakthrough time of the primary recycled adsorbent is 330 min, while that of the secondary recycled adsorbent is less than 210 min. It is indicated that the stability of the adsorbent is less than satisfactory, which might be caused by the irreversible adsorption of part of CO_2 on the Zn-13X. This resulted in a gradual reduction in the number of active sites.

Figure 11 shows the Fourier transform infrared spectroscopy (FTIR) of blank 13X, fresh Zn-13X, used Zn-13X, regenerated Zn-13X and used Zn-13X after regeneration. The blank 13X and fresh Zn-13X samples show quite similar spectra. Specifically, the adsorption peaks at $720\text{--}650\text{ cm}^{-1}$ and $950\text{--}1250\text{ cm}^{-1}$ are classified into symmetric stretch and asymmetric stretch, respectively. In the FTIR spectra of the samples, the adsorption events at $3420\text{--}3300\text{ cm}^{-1}$ and 1640 cm^{-1} are attributed to the O-H vibration caused by incomplete

dehydration of the molecular sieve samples [31,32]. However, the FTIR spectra show clearly that the peak of O-H vibration is gradually weakened to disappear after the activation and regeneration of the adsorbent, indicating that the molecular sieve is inevitably dehydrated by hydroxyl condensation at 450 °C. This is consistent with the previous simultaneous thermal analysis. The weakening of physical adsorption due to dehydroxylation is the first reason for the deteriorating regeneration performance of the adsorbent.

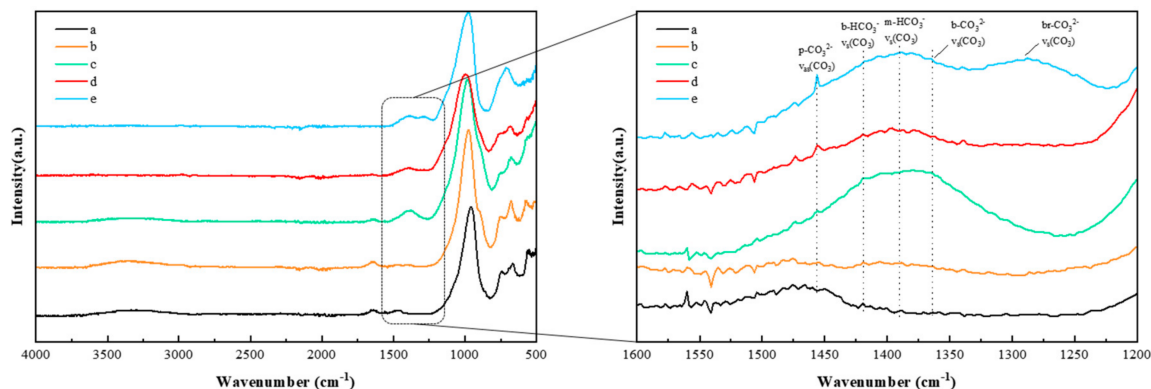


Figure 11. The infrared spectra of different adsorbents were as follows: (a) blank 13X, (b) fresh Zn-13X, (c) used Zn-13X, (d) regenerated Zn-13X and (e) used Zn-13X after regeneration.

The FTIR results obtained at 1600–1200 cm^{-1} indicate that the presence of CO_2 over Zn-13X adsorption leads to the formation of bicarbonate and carbonate species [33]. The peaks are 1456, 1419, 1390, 1365 and 1294 cm^{-1} , respectively. This is attributed not only to the ν_s vibration modes of bidentate and monodentate bicarbonate (1419 and 1390 cm^{-1} , respectively), but also to the ν_s vibration modes of bidentate and bridged carbonate (1365 and 1294 cm^{-1} , respectively). Differently, the extra peak at 1456 cm^{-1} is ascribed to the polydentate carbonate. Notably, there are several carbonate signals of regenerated Zn-13X that have different trends compared with the FTIR spectra after adsorption. The signal strength of polydentate carbonate and bridged carbonate increases and remains unchanged after regeneration. By contrast, the signals of carbonate and bicarbonate in other forms are weakened to different degrees after regeneration. That is to say, bidentate, monodentate bicarbonate, and bidentate carbonate can be decomposed to different degrees after regeneration. The signal of all carbonate species is enhanced after adsorption by the regenerated adsorbent, and that of polydentate carbonate is evident.

Through the above analysis, it can be concluded that carbonates are not completely decomposed after regeneration, thus resulting in a gradual decrease in the number of reactive oxygen species sites capable of absorbing CO_2 after regeneration. Additionally, this phenomenon becomes more obvious with the extension of regeneration times. The gradual weakening of chemical adsorption caused by this phenomenon is another reason for the poor regeneration performance of the adsorbent.

3.3. Mechanism of Adsorption

CO_2 reacts with ZnO in a wide variety of products. Based on Tang's density flooding theory plus the U (DFT + U) method under periodic boundary conditions, the intensity of CO_2 adsorption on the surface of different ZnO varies. The stability of the carbonates formed is in decreasing order as follows: polydentate, bridged, bidentate and monodentate carbonate [34], which is similar to the present study of experimental adsorbent regeneration. Additionally, a significant amount of desorption occurs only for the monodentate and bidentate carbonate species after regeneration in this experiment. Figure 12 shows the adsorption and desorption processes as observed in this experiment. There are five carbonate species produced on the adsorbent after CO_2 adsorption, as the 13X has a hydroxyl-rich surface, which facilitates the production of bicarbonate. However, some carbonate species

are irreversibly adsorbed onto the adsorbent due to limitations in their differential stability. According to Du et al., only polydentate carbonate could not be decomposed at high temperatures by the adsorption of CO_2 on K-promoted hydrotalcite-like compound (HTlc), which is slightly inconsistent with the results of this experiment. This difference is attributed to the insufficient regeneration time in this experiment and the high stability of the bridging carbonate. However, extending the regeneration would lead to severe dehydration in 13X. Furthermore, according to some studies, the increase in polydentate carbonate content during desorption in this experiment could result from the gradual conversion of other carbonate species into polydentate carbonate at high temperatures [35]. This is coherent with the common sense that matters tend to be transformed into more stable products.

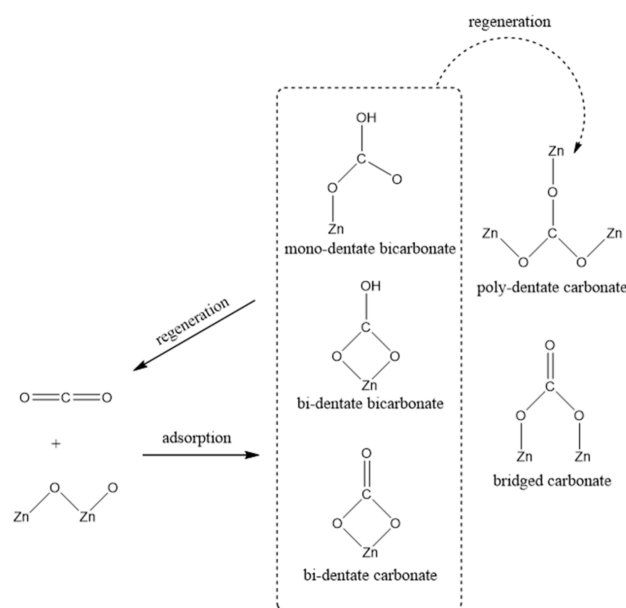


Figure 12. Schematic diagram of CO_2 adsorption and desorption.

4. Conclusions

The optimum carrier 13X and the optimum loading $\text{Zn}(\text{NO}_3)_2$ were determined by measuring alkalinity and performing BET and EDS characterization, respectively. The optimum concentration of impregnating solution and activation temperature required for preparing $\text{Zn}(\text{NO}_3)_2$ -13X were determined by means of SEM and TG-DSC characterization, respectively. After modification, the specific surface area, pore size and pore volume of 13X were reduced. To avoid agglomeration on the surface of 13X, $\text{Zn}(\text{NO}_3)_2$ should be kept at a low concentration during impregnation. It is inevitable that the complete decomposition of $\text{Zn}(\text{NO}_3)_2$ on 13X leads to the hydroxyl condensation and dehydration of 13X.

The CO_2 adsorption capacity of each sample in the CO_2/BF_3 gas mixture was determined by conducting dynamic adsorption breakthrough experiments. The chemical adsorption of CO_2 was confirmed through regeneration experiments and FTIR characterization of the samples before and after regeneration. It was also revealed in the study that the adsorption behavior of CO_2 on the Zn-13X surface gave rise to five carbonate species, of which bicarbonate may be formed by the incorporation of CO_2 molecules into the hydroxyl groups on the adsorbent surface. During the adsorption process after regeneration, some less basic sites (i.e., surface carbonates) were irreversibly converted into highly basic sites (i.e., active sites), which is due to the high stability of bridged and polydentate carbonate and the conversion of monodentate and bidentate carbonate species into polydentate carbonate during regeneration. In addition, the continuous dehydration of 13X during the regeneration process caused a deterioration in the adsorption property of the sample after regeneration.

In this study, BF_3 was diluted to a lower concentration using N_2 to reduce the risk of the experiment. This practice may lead to deviations between the effects of the adsorbent in industrial applications and the results of this study. Therefore, the concentration of BF_3 in raw gas can be increased as much as possible in order to be close to the actual industrial production. In addition, the poor thermal stability of 13X in the adsorbent stability evaluation in this study is inconsistent with the high thermal stability of polydentate and bridged carbonates, meaning that high regeneration temperatures disrupt the structure of 13X and low regeneration temperatures prevent partial carbonate decomposition. Therefore, it is possible to find a balance between the two, seek the optimum temperature for regeneration, or select a carrier with better thermal stability.

Author Contributions: Conceptualization, G.H.; methodology, Z.H.; formal analysis, Z.H.; investigation, Z.H.; resources, G.H.; data curation, Z.H.; writing—original draft preparation, Z.H.; writing—review and editing, G.H.; visualization, Z.H.; project administration, G.H. All authors have read and agreed to the published version of the manuscript.

Funding: This research received no external funding.

Data Availability Statement: Research data have been provided in the manuscript.

Conflicts of Interest: The authors declare no conflict of interest.

References

1. Tsukamoto, K.; Kuroi, T.; Kawasaki, Y. Evolution of Ion Implantation Technology and its Contribution to Semiconductor Industry. In Proceedings of the 18th International Conference on Ion Implantation Technology, Kyoto, Japan, 6–11 June 2010; pp. 9–16.
2. Graham, C.; Imrie, D.A.; Raab, R.E. Measurement of the electric quadrupole moments of CO_2 , CO , N_2 , Cl_2 and BF_3 . *Mol. Phys.* **1998**, *93*, 49–56. [[CrossRef](#)]
3. Volker, J.; Gernot, F.; Manfred, T.R. Comparative Theoretical Study of Lewis Acid-Base Complexes of BH_3 , BF_3 , BCl_3 , AlCl_3 , and SO_2 . *J. Am. Chem. Soc.* **1994**, *116*, 8141–8753. [[CrossRef](#)]
4. Snuffin, L.L.; Whaley, L.W.; Yu, L. Catalytic Electrochemical Reduction of CO_2 in Ionic Liquid EMIMBF₃Cl. *J. Electrochem. Soc.* **2011**, *158*, F155–F158. [[CrossRef](#)]
5. Choi, M.; Lyons, J.L.; Janotti, A.; Van de Walle, C.G. Impact of carbon and nitrogen impurities in high-kappa dielectrics on metal-oxide-semiconductor devices. *Appl. Phys. Lett.* **2013**, *102*, 4. [[CrossRef](#)]
6. Taeck-Hong, L.; Jae-Young, K. Study for an BF_3 Specialty Gas Production. *J. Korean Inst. Gas* **2011**, *15*, 74–78.
7. Asghar, U.; Rafiq, S.; Anwar, A.; Iqbal, T.; Ahmed, A.; Jamil, F.; Khurram, M.S.; Akbar, M.M.; Farooq, A.; Shah, N.S.; et al. Review on the progress in emission control technologies for the abatement of CO_2 , SO_x and NO_x from fuel combustion. *J. Environ. Chem. Eng.* **2021**, *9*, 106064. [[CrossRef](#)]
8. Pour, A.A.; Sharifnia, S.; NeishaboriSalehi, R.; Ghodrati, M. Performance evaluation of clinoptilolite and 13X zeolites in CO_2 separation from CO_2/CH_4 mixture. *J. Nat. Gas Sci. Eng.* **2015**, *26*, 1246–1253. [[CrossRef](#)]
9. Mofarahi, M.; Gholipour, F. Gas adsorption separation of CO_2/CH_4 system using zeolite 5A. *Microporous Mesoporous Mater.* **2014**, *200*, 1–10. [[CrossRef](#)]
10. Nagase, T.; Miyakawa, M.; Nishioka, M.; Ikeda, T. Microwave-assisted Green Synthesis of Mesoporous Zeolite Adsorbents for Direct Air Capture of CO_2 . *Chem. Lett.* **2022**, *51*, 296–299. [[CrossRef](#)]
11. Shen, J.; Sun, Q.; Cao, J.; Wang, P.; Jia, W.L.; Wang, S.Y.; Zhao, P.; Wang, Z.P. A lamellar structure zeolite LTA for CO_2 capture. *New J. Chem.* **2022**, *46*, 6720–6728. [[CrossRef](#)]
12. Shekhah, O.; Belmabkhout, Y.; Chen, Z.; Guillerm, V.; Cairns, A.; Adil, K.; Eddaoudi, M. Made-to-order metal-organic frameworks for trace carbon dioxide removal and air capture. *Nat. Commun.* **2014**, *5*, 4228. [[CrossRef](#)]
13. Guclu, Y.; Erer, H.; Demiral, H.; Zorlu, Y.; Altintas, C.; Keskin, S.; Semerci, F. Two-dimensional oxalamide based isostructural MOFs for CO_2 capture. *J. Solid State Chem.* **2023**, *319*, 6. [[CrossRef](#)]
14. Park, J.M.; Lim, S.; Park, H.; Kim, D.; Cha, G.Y.; Jo, D.; Cho, K.H.; Yoon, J.W.; Lee, S.K.; Lee, U.H. CO_2 capture performance of fluorinated porous carbon composite derived from a zinc-perfluoro metal-organic framework. *Sep. Purif. Technol.* **2022**, *302*, 12. [[CrossRef](#)]
15. Zhang, W.; Guo, Y.; Xu, J.; Wang, X. Purification process of boron trifluoride by cryogenic distillation. *Mod. Chem. Ind.* **2014**, *34*, 137–141.
16. Rajoria, D.S. Purification of Gaseous Inorganic Halide. US-6790419-B1, 14 September 2004.
17. Lee, J.Y.; Choi, H.Y.; Song, H.D.; Jeong, S.J.; Hwang, D.H. Method of Purifying Boron Trifluoride Involves Removing Impurities from in Low-Boiling Point of Boron Fluoride Target by Carbon Dioxide Adsorption, and Separating Low-Boiling Impurities Except Fluorinated Boron. KR1202421-B1, 16 November 2012.

18. Fashi, F.; Ghaemi, A.; Behroozi, A.H. Piperazine impregnation on Zeolite 13X as a novel adsorbent for CO₂ capture: Experimental and modeling. *Chem. Eng. Commun.* **2021**, *208*, 1104–1120. [[CrossRef](#)]
19. Lee, S.K.; Han, S.W.; Cha, G.Y.; Park, J.M.; Park, H.; Ryoo, R.; Lee, U.H. Base-type nitrogen doping in zeolite-templated carbon for enhancement of carbon dioxide sorption. *J. CO₂ Util.* **2022**, *62*, 10. [[CrossRef](#)]
20. Kato, M.; Yoshikawa, S.; Nakagawa, K. Carbon dioxide absorption by lithium orthosilicate in a wide range of temperature and carbon dioxide concentrations. *J. Mater. Sci. Lett.* **2002**, *21*, 485–487. [[CrossRef](#)]
21. Stefanelli, E.; Vitolo, S.; Puccini, M. Single-step fabrication of templated Li₄SiO₄-based pellets for CO₂ capture at high temperature. *J. Environ. Chem. Eng.* **2022**, *10*, 10. [[CrossRef](#)]
22. Jonnalagadda, M.; Ibrahim, S.M.; Shair, O.H.M.; Mutyala, S. Porous carbon supported calcium oxide for CO₂ adsorption and separation of CO₂/CH₄. *Environ. Technol.* **2022**, *43*, 460–468. [[CrossRef](#)]
23. Wang, F.; Gunathilake, C.; Jaroniec, M. Development of mesoporous magnesium oxide–alumina composites for CO₂ capture. *J. CO₂ Util.* **2016**, *13*, 114–118. [[CrossRef](#)]
24. Pang, H.; Xu, H.R.; Sun, A.W.; Xiao, G. Characteristics of MgO-based sorbents for CO₂ capture at elevated temperature and pressure. *Appl. Surf. Sci.* **2022**, *598*, 10. [[CrossRef](#)]
25. Taira, K.; Nakao, K.; Suzuki, K. CO₂ capture in humid gas using ZnO/activated carbon and ZnO reactivity with CO₂. *Reaction Kinet. Mech. Catal.* **2015**, *115*, 563–579. [[CrossRef](#)]
26. Li, W.; Jiang, X.; Yang, H.; Liu, Q. Solvothermal synthesis and enhanced CO₂ adsorption ability of mesoporous graphene oxide-ZnO nanocomposite. *Appl. Surf. Sci.* **2015**, *356*, 812–816. [[CrossRef](#)]
27. Pelech, I.; Staciwa, P.; Sibera, D.; Kusiak-Nejman, E.; Morawski, A.W.; Kapica-Kozar, J.; Narkiewicz, U. The Effect of the Modification of Carbon Spheres with ZnCl₂ on the Adsorption Properties towards CO₂. *Molecules* **2022**, *27*, 19. [[CrossRef](#)] [[PubMed](#)]
28. Wang, S.; Wang, Y.; Kuang, Y.; Xu, S.; Gao, S.; Liu, L.; Niu, H.; Xiao, P.; Huang, B. Adsorption behaviour of molecular sieve and activated carbon for CO₂ adsorption at cold temperatures. *Carbon Neutrality* **2022**, *1*, 16. [[CrossRef](#)]
29. Rehman, A.; Park, S.J. Tunable nitrogen-doped microporous carbons: Delineating the role of optimum pore size for enhanced CO₂ adsorption. *Chem. Eng. J.* **2019**, *362*, 731–742. [[CrossRef](#)]
30. Xu, X.; Huang, G. Effect of 13X Zeolite Modified with CuCl₂ and ZnCl₂ for Removing Phosphine from Circular Hydrogen of a Polysilicon Chemical Vapor Deposition Stove. *Ind. Eng. Chem. Res.* **2016**, *55*, 1380–1386. [[CrossRef](#)]
31. Valkaj, K.M.; Katovic, A.; Zrncevic, S. Catalytic Properties of Cu/13X Zeolite Based Catalyst in Catalytic Wet Peroxide Oxidation of Phenol. *Ind. Eng. Chem. Res.* **2011**, *50*, 4390–4397. [[CrossRef](#)]
32. Bandarchian, F.; Anbia, M. Conventional hydrothermal synthesis of nanoporous molecular sieve 13X for selective adsorption of trace amount of hydrogen sulfide from mixture with propane. *J. Nat. Gas Sci. Eng.* **2015**, *26*, 1380–1387. [[CrossRef](#)]
33. Koeck, E.-M.; Kogler, M.; Bielz, T.; Kloetzer, B.; Penner, S. In Situ FT-IR Spectroscopic Study of CO₂ and CO Adsorption on Y₂O₃, ZrO₂, and Yttria-Stabilized ZrO₂. *J. Phys. Chem. C* **2013**, *117*, 17666–17673. [[CrossRef](#)]
34. Tang, Q.-L.; Luo, Q.-H. Adsorption of CO₂ at ZnO: A Surface Structure Effect from DFT+U Calculations. *J. Phys. Chem. C* **2013**, *117*, 22954–22966. [[CrossRef](#)]
35. Du, H.; Williams, C.T.; Ebner, A.D.; Ritter, J.A. In Situ FTIR Spectroscopic Analysis of Carbonate Transformations during Adsorption and Desorption of CO₂ in K-Promoted HTlc. *Chem. Mater.* **2010**, *22*, 3519–3526. [[CrossRef](#)]

Disclaimer/Publisher’s Note: The statements, opinions and data contained in all publications are solely those of the individual author(s) and contributor(s) and not of MDPI and/or the editor(s). MDPI and/or the editor(s) disclaim responsibility for any injury to people or property resulting from any ideas, methods, instructions or products referred to in the content.